Contents list available at IJRED website

Int. Journal of Renewable Energy Development (IJRED)

Journal homepage: https://ijred.undip.ac.id

Research Article

The Effects of Dopant Concentration on the Performances of the a-SiO$_x$:H(p)/a-Si:H(i$_1$)/a-Si:H(i$_2$)/µc-Si:H(n) Heterojunction Solar Cell

Dadan Hamdani[a,*], Soni Prayogi[b], Yoyok Cahyono[c], Gatut Yudoyono[c], D. Darminto[c]

[a] *Department of Physics, FMIPA, Mulawarman University, Samarinda, 75123, Indonesia*

[b] *Department of Physics, FMIPA, Syiah Kuala University, Banda Aceh, 23111, Indonesia,*

[c] *Department of Physics, FSAD, Institut Teknologi Sepuluh Nopember, Surabaya, 60111, Indonesia*

Abstract. In this work, the imbalances in band gap energy between p-window layer and intrinsic layer (p/i interface) in p-i-n type solar cells to suppress charge recombination adopting with the addition of buffer layer, at p/i interface, namely solar cell structures without buffer (Cell A) and with buffer (Cell B). Using well-practiced AFORS-HET software, performances of Cell A and Cell B structures are evaluated and compared to experimental data. A good agreement between AFORS-HET modelling and experimental data was obtained for Cell A (error = 1.02%) and Cell B (error = 0.07%), respectively. The effects of dopant concentrations of the p-type and n-type were examined with respect to cell B for better performance by analysing the energy band diagram, the electric field distribution, the trapped hole density, the light J-V characteristics, and the external quantum efficiency. The simulated results of an optimised Cell B showed that the highest efficiency of 8.81% (V_{OC} = 1042 mV, J_{SC} = 10.08 mA/cm^2, *FF* = 83.85%) has been obtained for the optimum dopant values of N_A = 1.0 x 10^{19} cm^{-3} and N_D = 1.0 x 10^{19} cm^{-3}, respectively. A comparison between experimental data and simulation results for Cell B showed that the conversion efficiency can be enhanced from 5.61% to 8.81%, using the optimized values.

Keywords: p-type, n-type, AFORS-HET, dopant concentration, p/i interface, efficiency

Article History: Received: 22nd July 2021; Revised: 25th Sept 2021; Accepted: 31st Oct 2021; Available online: 10th Nov 2021
How to Cite This Article: Hamdani, D., Prayogi, S., Cahyono, Y., Yudoyono, G. and Darminto, D. (2022) The Effects of Dopant Concentration on the Performances of the a-SiOx:H(p)/a-Si:H(i1)/a-Si:H(i2)/µc-Si:H(n) Heterojunction Solar Cell. *International Journal of Renewable Energy Development*, 11(1), 173-181
https://doi.org/10.14710/ijred.2022.40193

1. Introduction

The sun is one of the largest energy sources on earth and it is converted into electrical energy with photovoltaic (PV) technology which is expected to support the increasing needs. The continuous study and development of this scientific system in respect to different fabrication and techniques aim to improve their conversion efficiency (Kabbani & Shaik, 2021). Presently, the solar cells being developed, including thin-film silicon types received a lot of attention, as the next generation models, because it has several advantages, such as the availability of Si raw material, which is abundant in nature. Therefore, low-cost and efficient solar cells are continuously developed, to assess the economic viability of photovoltaic power generation (Cho *et al*., 2018). The thin-film types have been the subject of extensive study for several decades as solar energy-harvesting devices, whereas presently the highest efficiencies for a-Si:H (triple-junction), CIGS, and CdTe are 14.04%, 23.35%, and 22.1%, respectively (Efaz *et al*., 2021).

Its conversion efficiency is enhanced by utilizing high-quality p-window and intrinsic layers. Furthermore, from the device standpoint, the p/i interface also plays a crucial role in reducing the mismatch bandgap and minimizing charge carrier recombination. The trap centers at the p/i interface appear at the internal electric field distribution due to its localized state (Hamdani *et al*., 2021). The optoelectronic properties of the p-i-n structure silicon thin-film solar cells depend on the quality of the layered window which affects the overall performance. The use of materials with a wide bandgap is the solution to improve the optical and electrical properties (Park *et al*., 2013). Moreover, a-SiOx:H film is widely used as the p-window layer, due to its characteristics, especially a wide bandgap (>1.9 eV), lesser conductivity (<10^{-6} S/cm), and high activation energy (0.6 eV), which are suitable for solar cell applications (Ahmad *et al*., 2017; Choi *et al*., 2019; Park *et al*., 2015).

However, the a-SiO$_x$:H(p)/a-Si: H(i) interface is related to higher built-in potential (V_{bi}), greater V_{OC}, and also spectral responses at the blue region of the spectrum, which was enhanced due to the extremely transparent material with wide bandgap. Furthermore, due to the different values for (p)- (~2.05 eV) and absorber layers

* Corresponding author: d.hamdani1973@gmail.com

(~1.72 eV), bandgap discontinuity is likely to occur at the p/i interface, where a thin defective region is formed and acts as recombination loss of photogenerated carriers (Park *et al*., 2013). Certain methods have also been applied to diminish the recombination loss at the p/i interface by inserting a buffer between (p) and absorber layers, including carbon alloys, a-SiC:H (Myong & Lim, 2005), silicon oxide, a-SiO_x:H (Ahmad *et al*., 2017; Fang *et al*., 2014; Pham *et al*., 2018). This includes the intrinsic double layers with different bandgap (Choi *et al*., 2019; Prayogi *et al*., 2021).

In this study, the structure of the Glass/ITO/a-SiO_x:H(p)/a-Si:H(i_1)/a-Si:H(i_2)/μc-Si:H(n)/Ag solar cell designed by Choi *et al*., (2019), was investigated by applying numerical method, using the AFORS-HET simulator. The proposed structure consists of a wide bandgap a-SiOx:H and a-Si:H as p-window and buffer layers. This includes structure without and with buffer (Cell A) and (Cell B), respectively. The calculation was carried out to understand the influences of the inserted buffer and the dopant concentrations of the doped layers on the solar cells' output characteristics. The reasons for the high performances in terms of energy band diagrams, electric field distribution, trapped hole density, light J-V characteristics, and external quantum efficiency, for the proposed heterojunction solar cell, was analysed.

2. Solar cell structure and simulation details

2.1 Simulation approach

AFORS-HET is a 1D numerical simulated program, which is widely used to simulate heterojunction solar cells developed at the Helmholtz Zentrum Berlin (HZB). It is divided into two parts, namely optical and electrical simulations. The defect state distribution in accordance with the Shockley-Read-Hall (SRH) recombination statistics, the modelling of each bulk layer is calculated using the Poisson and continuity equations, for electrons and holes. In the steady-state, the mathematical model defines the electric transport within the semiconductor as expressed in Eqs. (1-3) (Ahmad *et al*., 2017; Qiao *et al*., 2016; Stangl *et al*., 2010).

$$\nabla^2.\psi = -\frac{\rho}{\varepsilon}$$

$$\nabla.J_p = q(G-R) \quad (2)$$

$$\nabla.J_n = -q(G-R) \quad (3)$$

where q is electron charge, ε is the electric constant, ψ is the electric potential, G and R are generation and recombination rate, respectively, ρ is the net charge carrier density as expressed in Eq. (4).

$$\rho = p - n + N_D^+ - N_A^- + N_{TD} + N_{DB} \quad (4)$$

where p and n are the free holes and electron concentration, N_D^+, and N_A^- are ionized donors and acceptors concentration, N_{TD} and N_{DB} are trapped electrons and holes in the tail as well as dangling bond states, respectively. The current densities of the electron and hole from Eqs. (2,3) are stated in eqs. (5-6).

$$J_p = -q\mu_p p\nabla\psi - kT\mu_p\nabla p \quad (5)$$

$$J_n = -q\mu_n n\nabla\psi - kT\mu_n\nabla n \quad (6)$$

where μ_p and μ_n are hole and electron mobilities, respectively.

The defect states in amorphous material present within the band gap with localized DOS strongly influence the solar cell. In the simulation, the DOS models control the trapp carrier density and recombination center within the space charge distribution. These defect states mainly consist of exponential band-tail states and deep dangling-bon (DB). The total defect density of conduction band-tail (acceptor-like) N_{C-tail} and valence band-tail (donor-like) N_{V-tail} within energy distribution E is stated in Eqs. (6,7) (Hua *et al*., 2012):

$$N_{C-tail}(E) = \int_{E_V}^{E_C} N_{OC} exp\left(\frac{E-E_C}{E_{OC}}\right) dE \quad (7)$$

$$N_{V-tail}(E) = \int_{E_V}^{E_C} N_{OV} exp\left(\frac{E_C-E}{E_{OV}}\right) dE \quad (8)$$

where N_{OC} and N_{OV} are the densities per energy range at the conduction and valence band edges, E_{OC} and E_{OV} are inverse logaritmic slope (Urbach energies) of the conduction and valence bands, respectively. The N_{OC} and N_{OV} values taken from 2.0 x 10^{21} – 4.0 x 10^{21} cm^{-3}/eV and vary with doping concentration (Schmidt *et al*., 2004).

The DB defect states lies near the mid-gap as recombination centers result from dangling sp-hybrid orbtals of Si atoms. The DB states are continuously distributed in forms as two Gaussian distribution functions and can have three charge states, namely netral state (D^0), positively charged (D^0/D^+), and negatively charged (D^-/D^0). The donor-like and acceptor-like densities can be described by Eqs. (9,10) (Hua *et al*., 2012)

$$N_{tD}(E) = \int_{E_V}^{E_C} N_{DO} exp\left(-\frac{\left(E-E^{0/+}\right)^2}{2\left(FWHM/_2\right)^2}\right) dE \quad (9)$$

$$N_{tA}(E) = \int_{E_V}^{E_C} N_{AO} exp\left(-\frac{\left(E-E^{-/0}\right)^2}{2\left(FWHM/_2\right)^2}\right) dE \quad (10)$$

where N_{DO} and N_{A0} are the peak of defect states that are associated with D^0/D^+ and D^-/D^0 transitions, respectively, with $E^{0/+}$ and $E^{-/0}$ are the peak energy positions beyond E_V and FWHM is the full width at half maximum of the Gaussian distribution functions.

In this simulation, the DB density was calculated using the defect pool model developed by Powell and Dean. The analytical expression for this model as expressed in Eq. (11) (Bouhdjar *et al*., 2015):

$$D(E) = \gamma\left(\frac{2}{f^0(E)}\right)^{k_BT*/2E_{v0}} P\left(E + \frac{FWHM^2}{2E_{v0}}\right) \quad (11)$$

where γ is scalling factor can be written in eq. (12):

$$\gamma = \left(\frac{G_v 2E_{v0}^2}{(2E_{v0} - k_B T)}\right)\left(\frac{H}{N_{SiSi}}\right)^{k_B T^*/4E_{v0}} x\ exp\left(-\frac{1}{2E_{v0}}\left(E_p - E_v - \frac{FWHM^2}{4E_{v0}}\right)\right) \quad (12)$$

where $P(E)$ is the defect pool function (Gaussian distribution), E_p is the most probable energy for defect formation, H is the total hydrogen concentration amorphous materials, N_{SiSi} is the total number of electrons in silicon bonding, and T^* is the equilibrium freeze-in temperature.

In this model, the optical generation rate of carriers (electrons and holes), with photon flux density $\Phi^0(\lambda)$ of wavelength λ and device thickness d is stated in Eq. (13) (Ahmad *et al*., 2017):

$$G(x) = \int_d \int_\lambda \alpha(x,\lambda)\Phi^0(\lambda)\, x\,(1 - R(\lambda))exp(-\alpha(x,\lambda))dxd\lambda \quad (13)$$

where $\alpha(x)$ is the absorption coefficients of the layer, $R(\lambda)$ is reflectivity at the surface of the glass/TCO/(p)-layer structure.

Furthermore, the recombination process and trapping of a model in the case of amorphous material is described by the sum of the recombination rate through a single level trap, the tail, and DB states (D^+, D^0, D^-). Therefore, the total recombination rate is expressed in Eq. (14).

$$R_{total}(x) = R_{SRH}(x) + R_{TD}(x) + R_{DB}(x) \quad (14)$$

where $R_{SRH}(x)$ is the recombination rate through single level trap, $R_{TD}(x)$ and $R_{DB}(x)$ are recombination rate of tail states and DB states, respectively.

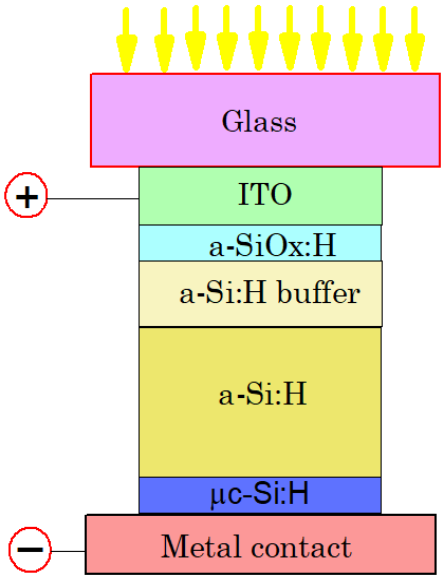

Fig.1 Sketch of proposed of the heterojunction solar cell structure Glass/ (ITO)/a-SiO_x:H(p)/a-Si:H(i_1)$_{buffer}$/a-Si:H(i_2)/µc-Si:H(n)/Ag.

2.2 Device structure and input parameters

Fig. 1 denotes the schematic diagram for the heterojunction solar cell structure Glass/TCO(ITO)/a-SiO_x:H(p)(20nm)/a-Si:H(i_1)$_{buff}$(20nm)/a-Si:H(i_2)(180nm)/µc-Si:H(n)(30nm)/Ag was deposited on soda-lime glasses using plasma-enhanced chemical pavor deposition (PECVD) reactor. The optoelectronic properties of the intrinsic films were tested with various hydrogen dilution (R) = [H_2]/[SiH_4] = 4 and 12, meanwhile, the results were adopted from the study carried out by Choi *et al*. Meanwhile, the doped (a-SiOx:H (p) and µc-Si:H(n)) layers were also deposited using PECVD reactor with gas mixtures of B_2H_6 (diborane) and PH_3 (phosphine) for doping in addition to SiH_4 (silane), hydrogen (H_2), and CO_2 at a temperature as low as 150 ^{0}C. To depress charge recombination at the p/i interface, the buffer layer (a-Si:H) was added to p-i-n-type structure to relieve the band gap mismatch between the p-window and absorber layers (p-i_1-i_2-n-type) using various hydrogen dilution. Moreover, as light sources, the radiation AM1.5G spectrum with 100 mW/cm^2 power density and 300 K operational temperature was used.

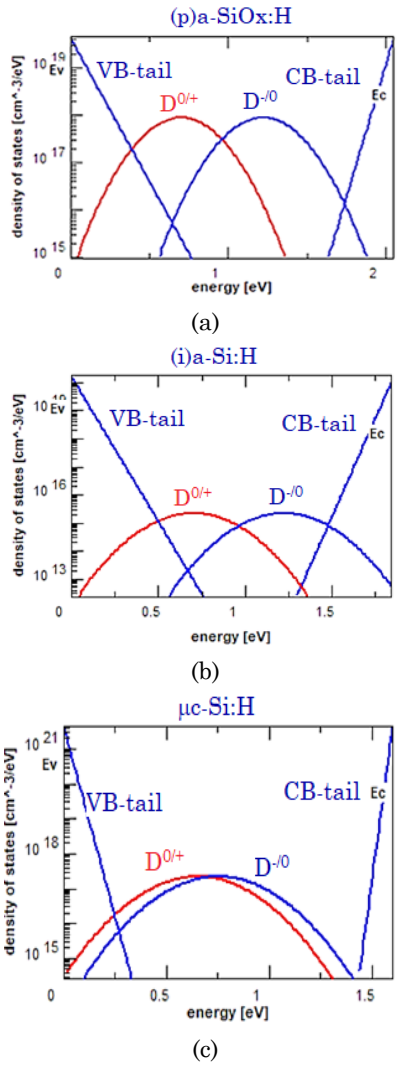

Fig. 2 The gap states distribution of (a) a-SiOx:H layer, (b) a-Si:H, and (c) µc-Si:H. $D^{0/+}$ and $D^{-/0}$ denotes donor-like DB and acceptor-like DB, respectively.

Table 1
Some input parameters for AFORS-HET simulator

Parameters	**(p)a-SiOx:H**	**(i_1)a-Si:H buffer**	**(i_2)a-Si:H**	**(n)μc-Si:H**
d (nm)	20	20	180	30
ε_r	11.9	11.9	11.9	11.9
χ (eV)	3.90	4.05	3.8	4
E_G (eV)	2.05	1.90	1.78	1.60
N_C (cm^{-3})	2.0×10^{20}	2.0×10^{20}	2.0×10^{20}	2.0×10^{20}
N_V (cm^{-3})	2.0×10^{20}	2.0×10^{20}	2.0×10^{20}	2.0×10^{20}
μ_e (cm^2/Vs)	7.85	9.78	9.78	30
μ_h (cm^2/Vs)	3.14	3.14	3.14	6
N_A (cm^{-3})	1.0×10^{18}	0	0	0
N_D (cm^{-3})	0	0	0	1.0×10^{19}
Tail states				
N_{OC} (cm^{-3}/eV)	1.5×10^{20}	1.0×10^{20}	1.0×10^{20}	4.0×10^{21}
N_{OV} (cm^{-3}/eV)	1.5×10^{20}	1.0×10^{20}	1.0×10^{20}	4.0×10^{21}
E_{OC} (eV)	0.04	0.03	0.03	0.04
E_{OV} (eV)	0.07	0.04	0.04	0.07
σ_{de} (cm^{-2})	2.5×10^{-15}	2.5×10^{-15}	2.5×10^{-15}	1.0×10^{-16}
σ_{dh} (cm^{-2})	2.0×10^{-14}	2.0×10^{-14}	2.0×10^{-14}	1.0×10^{-15}
σ_{ae} (cm^{-2})	2.0×10^{-14}	2.0×10^{-14}	2.0×10^{-14}	1.0×10^{-15}
σ_{ah} (cm^{-2})	2.5×10^{-15}	2.5×10^{-15}	2.5×10^{-15}	1.0×10^{-16}
Dangling-bond states				
N_{DO} (cm^{-3})	3.98×10^{17}	2.35×10^{16}	2.35×10^{16}	1.0×10^{17}
N_{AO} (cm^{-3})	3.98×10^{17}	2.35×10^{16}	2.35×10^{16}	1.0×10^{17}
E_{DO} (eV)	1.22	1.22	1.22	1.22
$E_{A)}$ (eV)	0.70	0.70	0.70	0.70
σ_{de} (cm^{-2})	1.0×10^{-14}	1.0×10^{-14}	1.0×10^{-14}	1.0×10^{-15}
σ_{dh} (cm^{-2})	1.0×10^{-15}	1.0×10^{-15}	1.0×10^{-15}	1.0×10^{-16}
σ_{ae} (cm^{-2})	1.0×10^{-15}	1.0×10^{-15}	1.0×10^{-15}	1.0×10^{-16}
σ_{ah} (cm^{-2})	1.0×10^{-14}	1.0×10^{-14}	1.0×10^{-14}	1.0×10^{-15}

The abbreviations in Table 1 are follows: d: thickness of the semiconductor layers, ε_r: dielectric constant, χ: electrons affinity, Eg: band gap, N_C: effective conduction band density, N_V: effective valence band density, μ_e: electron mobility, μ_h: hole mobility, N_A: acceptor doping, N_D: donor doping, N_{OC}/N_{OV}: exponential prefactors of donor-like or acceptor-like tail states, E_{OC}/E_{OV}: characteristic energy of the donor-like/acceptor-like tail states, σ_{de}, σ_{dh}: capture cross-section for donor states; σ_{ae}, σ_{ah}: capture cross-section for acceptor states, N_{DO}/N_{AO}: Gaussian density for donor and acceptor states, E_{DO}/E_{AO}: donor and acceptor Gaussian peak energy position.

The DOS distribution model in AFORS-HET for each heterojunction solar cell is described as the conduction-valence band-tails and the donor-acceptors such as DBs for -p, -i, and -n layers, as shown in Fig. 2 using equations 7 to 10. The results are obtained in Table 1 were generated with AFORS-HET software. Also, in hydrogenated silicon oxide, the energy values (Urbach energy) of 0.07 and 0.04 eV, were used by the donor and acceptor-like states, to generate a valence defect density and conduction band edges of approximately 1.5×10^{20} $cm^{-3}eV^{-1}$, the Gaussian was realized at 3.98×10^{17} cm^{-3}, with values of the carrier mobilities being 7.85 and 3.14 cm^2 1/Vs for electrons and holes. However, the defect densities of -i_2 and -n for both layers, are characterized with 2.35×10^{16} and 1.0×10^{17} cm^{-3}, respectively.

The TCO work function value which generates a neutral contact at ITO/p-window layer interface $WF_{TCO}^{n} = 5.40\ eV$ ($\varphi_{b0} = 1.50\ eV$) was used to carry out this research. Meanwhile, the work function at μc-Si:H(n)/Ag interface of the neutral back contact is WB_{TCO} = 4.2 eV ($\varphi_{bL} = 0.2\ eV$). Furthermore, the surface recombination velocities for electrons and holes were set at 1.0×10^7 cm/s. However, the dopant concentration of the p-window and n-layers varies from 1.0×10^{15} to 1.0×10^{23} cm^{-3}. The light reflection on the front and back contact (RF and RB) were set at both 0.05 and 0, respectively. This was based on the assumption that there was no back reflector on the simulated structure. The input parameters used in the simulation of cell B are shown in Table 1 (Ahmad *et al*., 2017; Choi *et al*., 2019; Hernández-Como and Morales-Acevedo, 2010; Kouider and Belfar, 2020).

3. Simulation results and discussion

3.1 Numerical validation of the heterojunction solar cells

According to Choi *et al*, 2019, several a-Si:H layer films have been developed with different band gap energy due to various R values, which are shown in Table 2. The Urbach energy would be decreased for higher R, which correlates to reduced defects (density of state) on the valence and conduction band tails and deep state defects (DB). The decrease in Urbach energy due to the increase in R causes band gap energy of (i)a-Si:H to increase. The increase of band gap energy is related to the effect of quantum confinement charge carriers, which indicates a change in the lattice from amorphous to nanoscale crystalline structure in the a-Si:H film according to the effective mass theory (Cahyono *et al*., 2018).

The imbalances in bandgap energy between p-window layer and intrinsic layers (p/i interface) in p-i-n type solar cells to suppress charge recombination adopting with

adding buffer layer p/i interface, namely solar cell structures without buffer (p-i_{R4}-n) and with buffer (p-i_{R12}-i_{R4}-n), as shown in Table 3. The bandgap energy and thickness of n-layer are 1.60 eV and 30 nm, respectively. Meanwhile, the solar cell structure without a buffer device was fabricated with intrinsic layer (R_4) thickness of 200 nm, whereas for solar cells with buffer layers thickness consisted sum of buffer layers' (20 nm) + absorber thickness layer (180 nm) = 200 nm.

The simulation results were compared using AFORS-HET software to experimental data from Choi *et al*, 2019 to evaluate the effect of the interface layer (buffer) on bandgap energy and solar cells performances, as shown in Table 3. In addition, the validity model was confirmed using Table 1. Referring to cell A (without buffer), a simulated efficiency of 4.85% suitably corresponds with the experimental result of 4.83%. Meanwhile, for cell B, after the insertion of the buffer layer (R=12) at the p/i interface, the efficiency of the simulated and measured output characteristics of the solar energy is improved by 5.61% and 5.57%, respectively, as shown in Table 4. The addition of a buffer layer on p-i-n solar cells causes bandgap energy imbalance (band offset) and repression charge recombination at the p/i interface which correlates with an increase in V_{OC} and *FF* values. The buffer layer causes a high internal electric field at this region, thereby sweeping out electron-hole pairs as well as minimizing recombination in the DRR (defect rich region) and the p/i interface. In addition, the charge carrier collection increases, in accordance with the performance of solar cell terraces (Ahmad *et al*, 2017).

Table 2
Variation of band gap energy of (p)a-SiOx:H and (i)a-Si:H layers with hydrogen values R = $[H_2]/[SiH_4]$ = 4 and 12.

Layers	Band gap energy (eV)
a-SiOx:H(p)	2.05
a-Si:H(i) (R=4)	1.78
a-Si:H(i) (R=12) buffer	1.90

Sources: Choi *et al*., 2019

Table 3
Set of p-i-n type heterojunction solar cells

Structures	Cells
a-SiOx:H(p)/R4/µc-Si:H(n) (p-i-n)	A
a-SiOx:H(p)/R12/R4/µc-Si:H(n) (p-i_1-i_2-n)	B

Table 4
Comparison of the experimental and simulation results of the solar cell without buffer (A) and with buffer (B).

Cells	V_{OC} (mV)	J_{SC} (mA/cm²)	*FF* (%)	E_{ff} (%)
Experimental A	855.0	9.56	59.10	4.83
AFORS-HET A	856.4	9.53	59.64	4.88
Error (%)	0.16	0.03	0.91	1.02
Experimental B	912.0	9.86	61.95	5.57
AFORS-HET B	915.5	9.81	62.48	5.61
Error (%)	0.38	0.51	0.85	0.07

3.2 Effect of the p-type and n-type dopants concentration to heterojunction solar cell performance

The subsequent discussion focuses on the analysis of the p-i_1-i_2-n structure (Cell B) because generally, it is better compared to the p-i-n (Cell A). The electric field which serves as a driving force for electrons and holes in the absorber of the p-i-n solar cell was generated by the p and n layers. Fig. 3(a) to (d) shows the external parameters (V_{OC}, J_{SC}, *FF*, and E_{ff}) of cell B with respect to the changes in the p-type doping concentration (N_A). Furthermore, this greatly affected the V_{OC} and *FF*, due to the influences of transition on resistance series and recombination loss, at the p/i interface (Lin *et al*., 2012).

Additionally, the effect of the p-type dopant concentration on the p/i_1 interface significantly terraced the V_{bi} (built-in potential), which causes an increase in V_{OC} and *FF* (885.9 to 915 mV and 68.98 to 82.80%) including N_A from 1.0 x 10^{17} to 1.0 x 10^{19} cm^{-3}, that further saturates after N_A > 1 x 10^{19} cm^{-3}. This was observed to be consistent with other studies (Dutta & Chatterjee, 2004; Jia *et al*., 2017). However, the values of J_{SC} decreases with N_A from 1.0 x 10^{17} to 1.0 x 10^{18} cm^{-3}, then slightly increased with the maximum value of 10.26 mA/cm^2 when the N_A of 1.0 x 10^{20} cm^{-3}, due to reduction of parasitic absorption in the p-p-window layer, therefore permanently decreased for heavily doped p-window layer. Based on this reason, the conversion efficiency (E_{ff}) value increased for high the p-type dopant concentration of 1.0 x 10^{19} cm^{-3} at 7.77% (maximum efficiency) and started to saturate at higher levels of the N_A. In the case of optimized structure, the value of N_A = 1.0 x 10^{19} cm^{-3} was used in this study.

Fig. 4(a) and (b) show the effect of N_D dopant concentration on the performance of cell B. It is evident that V_{OC} sharply increases when the N_D concentration was operated from 1.0 x 10^{17} to 1.0 x 10^{21} cm^{-3} in Fig. 4(a). The V_{OC} value is strongly determined by the N_A and N_D dopants concentration as shown in Eqs. (15,16) (Belfar, 2015; Jensen *et al*., 2002).

$$V_{OC} = \frac{V_{bi}}{q} - \frac{nkT}{q} ln\left(\frac{qN_V S_{it}}{J_{SC}}\right) \quad (15)$$

$$V_{bi} = \frac{kT}{q} ln\left(\frac{N_A N_D}{n_i^2}\right) \quad (16)$$

where V_{bi} is the built-in potential, N_V is the effective density of state in valence band, S_{it} is the interface recombination velocity, N_A and N_D are doping concentration of p-type and n-type, and n is intrinsic carrier concentration, respectively.

Furthermore, a slight decrease was detected in *the* J_{SC} value (Fig. 4(b)) with increasing N_D doping from 10.26 to 10.01 mA/cm^2. These results are illustrated by the band bending between the ITO/p-layer interfaces which are increased when the p-window is highly doped, as shown in Fig. 5. However, it is evident that the front barrier height (ϕ_{b0}) ITO/p-window layer changed due to the N_A dopant concentration. The changes in the N_A and N_D dopants concentrations caused the position of the Fermi energy level to move downward towards the valence and conduction bands. However, the barrier height in form of surface band-bending (E_{sbb}) hinders the photogenerated holes trying to exit the cell.

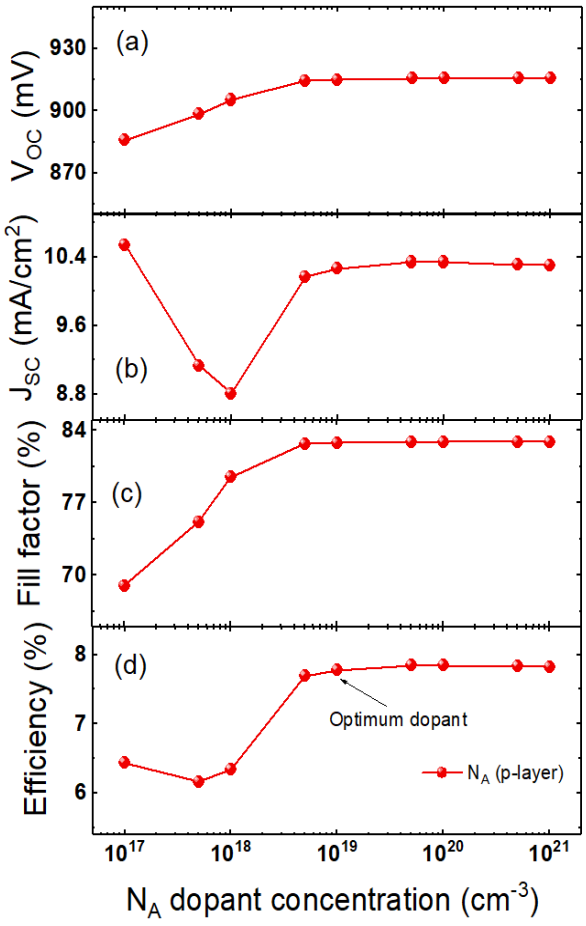

Fig. 3 External parameters of heterojunction solar cells (cell B): (a) V_{OC}, (b) J_{SC}, (c) Fill Factor, and (d) efficiency with variations p-type dopant concentration (N_A).

Meanwhile, the presence of the buffer layer accommodates the band offsets at the p/i interface, thereby reducing the trapped hole density and the recombination rate. Fig 4(c) showed that the fill factor (*FF*) also improved the N_D dopant concentration from 1.0 x 10^{17} to 1.0 x 10^{19} cm^{-3} about 82.80 to 83.85%, and was saturated to N_D > 1.0 x10^{19} cm^{-3}. According to Fig. 4(d), the conversion efficiency of cell B is improved by increasing N_D from 1.0 x 10^{17} to 1.0 x 10^{19} cm^{-3} (7.77 to 8.81%) at a constant of N_D > 1.0 x10^{19} cm^{-3}. Therefore, the results from the simulation stated that for better performances, the optimum N_D dopant concentration of the heterojunction solar cells was 1.0 x10^{19} cm^{-3}, with a maximum efficiency of 8.81%.

To provide an overview regarding the effect of changes in N_A and N_D dopant concentrations on the performance of heterojunction solar cell devices, it is important to analyse the electric field distribution and the trapped hole density, as depicted in Fig. 6(a) and (b). Furthermore, Fig. 6(a) shows a potential difference explained by variations in the distribution of the electric field, for four N_A dopant concentrations (N_D = 1.0 x 10^{19} cm^{-3}). It was observed that the electric field in the ITO/p-window layer interface was positive, which impedes that the photo-generated holes have attained the front contact. However, the strength of the electric field at the p/i_1 interface was diverse, depending on the different N_A dopant levels. For the doping level which is approximately 1.0 x 10^{19} cm^{-3}, the generated electric field at the p/i interface was observed to be weaker at 7.56 x 10^5 Vcm^{-1}, while the electric field strength was determined by p-window layer thickness. This indicates that the front surface field (FSF) resulted in an efficiency drop (Jia *et al.*, 2017). Meanwhile, when the dopant p-window layer concentration was increased to 1 x 10^{20} cm^{-3}, the electric field strength was also increased to 2.03 x 10^6 Vcm^{-1}, which was strong enough to permit the efficient accumulation of photogenerated charge carriers at both terminals. Moreover, when the dopant concentration was raised to 1.0 x 10^{21} cm^{-3}, the overly-strong electric field of 3.48 x 10^6 Vcm^{-1} generated a higher defect density at the p/i interface. This served as both recombination and trapping centres for charge carriers (Mehmood and Tauqeer, 2017). These results were confirmed by calculating the trapped hole densities for 3 N_A dopant concentrations, as shown in Fig. 6(b). It was observed that the trapped hole densities at p/i_1 interface increased with increasing N_A dopant concentration, i.e. 1.0 x 10^{19} cm^{-3} (4.52 x 10^{17} cm^{-3}), 1.0 x 10^{20} cm^{-3} (7.89 x 10^{17} cm^{-3}), and 1.0 x 10^{21} cm^{-3} (2.76 x 10^{18} cm^{-3}), respectively.

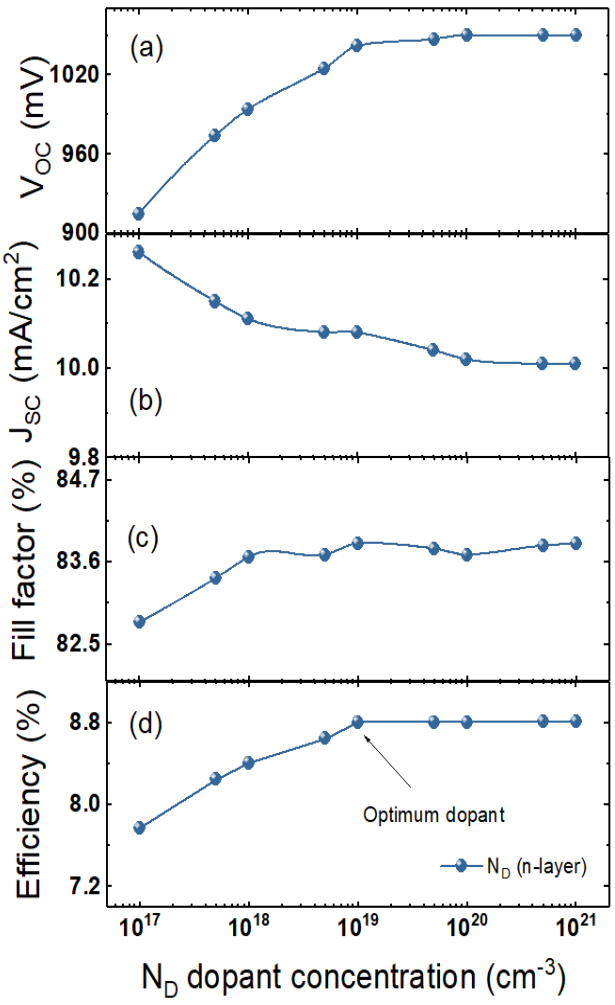

Fig. 4 External parameters of heterojunction solar cells (cell B): (a) V_{OC}, (b) J_{SC}, (c) Fill Factor, and (d) efficiency with variations n-type (N_D).

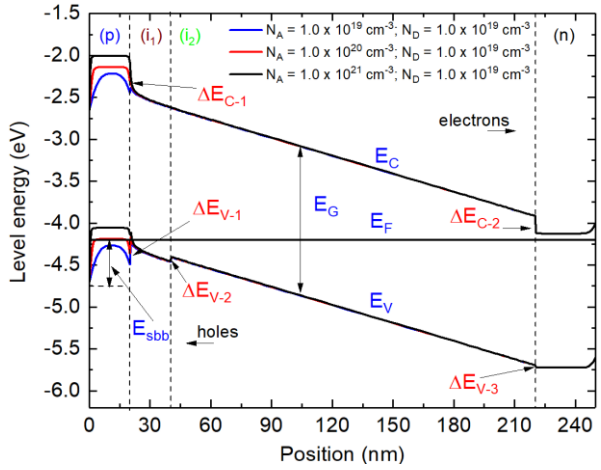

Fig. 5 Sketch of band diagrams of heterojunction solar cells due to change of the p-layer dopants for three levels (p)a-SiO_x:H layer dopant at Thermodynamics equilibrium.

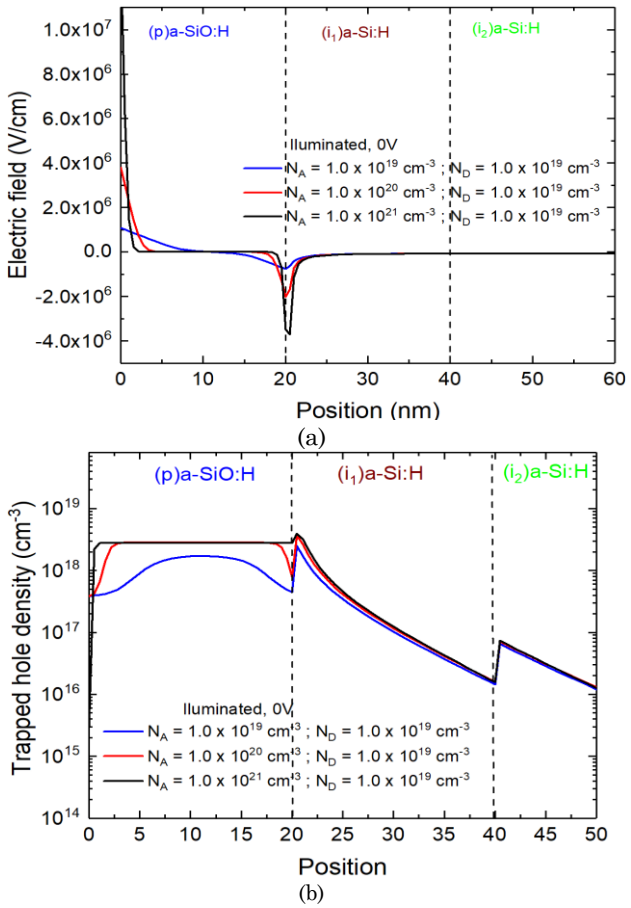

Fig. 6 (a) The electric field distribution, (b) the trapped hole densities for cell B with different N_A dopant concentration with N_D = 1.0 x 10^{19} cm^{-3} at short circuit current (V = 0V).

Fig. 7 depicts the J-V characteristics analysed under different N_A dopant concentrations used in the reference structure based on a-SiOx:H/a-Si:H solar cell (cell B), as shown in Table. 4. The simulated conversion efficiency of Cell B was calculated by AFORS-HET is 5.61% (V_{OC} = 915.5 mV, J_{SC} = 9.81 mA/cm^2, FF = 62.48%) was obtained and optimised by exploring different p-window (N_A) and n-layer (N_D) dopant concentrations. However, upon further optimization of dopant concentrations, the cell B numerically reached a conversion efficiency of 8.81% (V_{OC} = 1042 mV, J_{SC} = 10.08 mA/cm^2, FF = 83.85%) for the optimum dopant values of N_A = 1.0 x 10^{19} cm^{-3} and N_D = 1.0 x 10^{19} cm^{-3}, respectively.

Therefore, the influence of p-type dopant concentration on optical properties and photogenerated current of cell B, as depicted in Fig. 8 was examined and analysed. The photogenerated current J_{photo} indicated as J_{SC} in the short circuit condition was a description of the quantum efficiency, which is represented by Eqs. (16,17) (Hao *et al.*, 2019)

$$J_{SC} = \int_{300}^{800} \frac{q\lambda}{hc} \phi_{AM1.5}(\lambda) EQE(\lambda) d\lambda \qquad (16)$$

$$EQE(\lambda) = IQE\left(1 - R(\lambda)\right) \qquad (17)$$

where $h, c, \lambda, \phi_{AM1.5}, EQE, IQE, R$ are the Plank's constant, the speed of light, the wavelength, the solar spectral irradiance under air mass 1.5G, the external quantum efficiency, internal quantum efficiency, and reflectance, respectively.

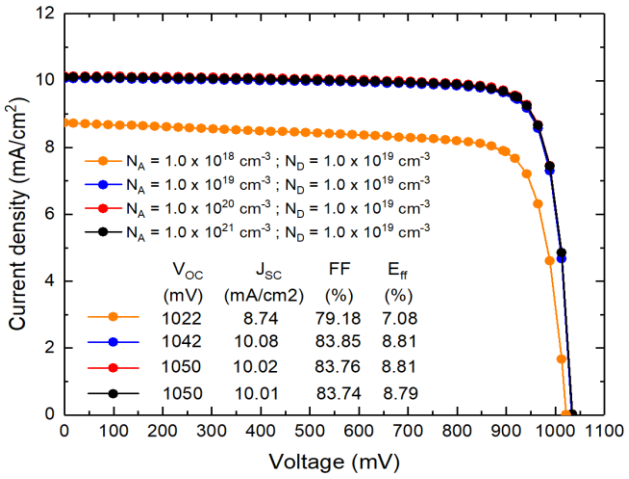

Fig. 7 The J-V characteristics of the cell B under illumination condition for different N_A dopant concentrations.

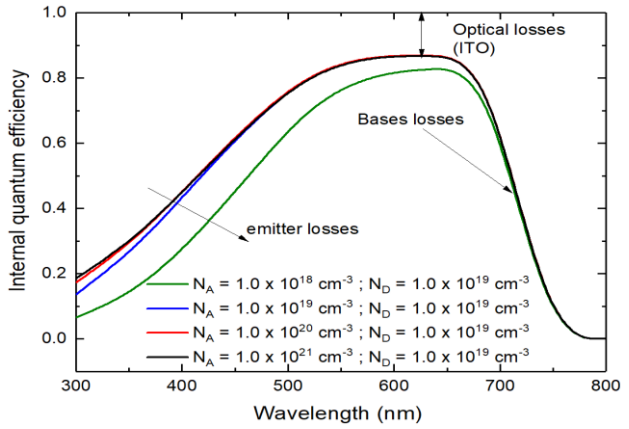

Fig. 8 The quantum efficiency of the Cell B for wavelength range from 300 to 800 nm with different N_A dopant concentrations.

Table 5
Simulated results of the Cell B using AFORS-HET sofware are compared with Silvaco TCAD (Ahmad *et al.*, 2017)

References	Buffer layer	V_{OC} (mV)	J_{SC} (mA/cm²)	*FF* (%)	E_{ff} (%)
TCAD	a-SiO:H	905.0	12.98	71.60	8.41
AFORS-HET	a-Si:H	925.5	12.64	72.81	8.52

Moreover, Fig. 8 showed the quantum efficiency of cell B with respect to changes to the dopant concentration of the p-window layer. It was also observed that when the dopant concentration was increased from 1.0 x 10^{17} to 1.0 x 10^{19} cm^{-3}, the spectrum wavelength of the quantum efficiency was also increased from 300 to 520 nm (blue region). This further proves that the dopant concentration had a good response in the blue region because the recombination at the p/i_1 layer interface was reduced. This indicates that the photogenerated charge carrier was efficiently extracted from the defect-rich region at the interface (Ahmad *et al.*, 2017). However, for the p-type dopant concentration > 1.0 x 10^{19} cm^{-3} (high dopant), it was observed that the quantum efficiency remains constant, which implies that the J_{SC} value is constant (Fig. 7).

Therefore, the simulation results of Cell B (with a-Si:H as a buffer) using AFORS-HET simulator, were compared to the solar cell using Silvaco TCAD (with a-SiO:H as a buffer) which employed identical parameters, as shown in Table 5 (Ahmad *et al.*, 2017).

4. Conclusion

In this study, a p-i-n solar cell based on the (p)a-SiOx:H-type and a-Si:H buffer layer have been numerically investigated and analysed using the AFORS-HET software. The p-i-n structures without (Cell A) and with buffer (Cell B) were studied and compared to determine the relevance of inserting interfacial layer (buffer) as well as to discover a realistic set of parameters for better solar cell performances. A good agreement was reached between AFORS-HET modelling and experimental data for Cells A (error = 1.02%) and B (error = 0.07%), respectively. The results show that the presence of a-Si:H buffer between the window and active (intrinsic) layers, at the p/i interface, improved the solar cell performances of cell B. This addition on the p-i-n causes bandgap energy imbalance (band offset) and repression charge recombination at the interface p/i which is correlated with an increase in V_{OC} and *FF* values.

The impacts of the p-type and n-type dopant concentrations in respect to Cell B performances were determined by calculating and analysing the energy band diagram, the electrical field distribution, the trapped hole density, the J-V characteristics, and the quantum efficiency. During optimization, the p-type (N_A) and the n-type (N_D) dopant concentrations, varied within the range of 1.0 x 10^{17} to 1.0 x 10^{21} cm^{-3}. It showed that Cell B has a high efficiency of 8.81% (V_{OC} = 1042 mV, J_{SC} = 10.08 mA/cm², *FF* = 83.85%) with an optimum dopant values of N_A = 1.0 x 10^{19} cm^{-3} and N_D = 1.0 x 10^{19} cm^{-3}, respectively. Finally, the simulated device was compared with the results obtained using AFORS-HET and Silvaco TCAD. Therefore, the proposed design for the heterojunction solar cell provided a reference for further technological development.

Acknowledgments

One of the authors (DH) would like to thankfully acknowledges to the Ministry of Finance for which provided the financial grant needed to carry out this research through BUDI-LPDP scholarship (Grant number: PRJ-5441/LPDP.3/2016). The authors are also grateful to HZB for the AFORS-HET Simulation Program.

References

Ahmad, G., Mandal, S., Barua, A.K., Bhattacharya, T.K., Roy, J.N., (2017). Band Offset Reduction at Defect-Rich p/i Interface Through a Wide Bandgap a-SiO:H Buffer Layer. IEEE Journal of Photovoltaics 7, 414–420. https://doi.org/10.1109/JPHOTOV.2016.2642644

Belfar, A., (2015). The role of p+-layer dopant concentration, p+-layer band gap and p+-layer thickness in the performances of a-Si:H n – i – p – p+ solar cells with double layer window nanocrystalline silicon. Optik 126, 5688–5693. https://doi.org/10.1016/j.ijleo.2015.09.026

Bouhdjar, A.F., Ayat, L., Meftah, AM, Sengouga, N., Meftah, AF, (2015). Computer modelling and analysis of the photodegradation effect in a-Si:H p—i—n solar cell. Journal of Semiconductors 36, 014002. https://doi.org/10.1088/1674-4926/36/1/014002

Cahyono, Y., Yahya, E., Zainuri, M., Pratapa, S., Darminto, (2018). Quantum Confinement in an Intrinsic a-Si:H Thin Film Deposited on Soda Lime Glass Substrate Using PECVD. Transactions on Electrical and Electronic Materials 19, 69–73. https://doi.org/10.1007/s42341-018-0002-3

Cho, J.-S., Jang, E., Lim, D., Ahn, S., Yoo, J., Cho, A., Park, J.H., Kim, K., Choi, B.-H., (2018). Wide-bandgap nanocrystalline silicon-carbon alloys for photovoltaic applications. Solar Energy Materials and Solar Cells 182, 220–227. https://doi.org/10.1016/j.solmat.2018.03.035

Choi, S.-W., Yang, J., Park, J.-H., Han, S.-J., Song, P., Kang, D.-W., Kwon, J.-D., (2019). P/i interfacial engineering in semi-transparent silicon thin film solar cells for fabrication at a low temperature of 150 °C. Current Applied Physics 19, 1120–1126. https://doi.org/10.1016/j.cap.2019.07.006

Dutta, U., Chatterjee, P., (2004). The open circuit voltage in amorphous silicon p-i-n solar cells and its relationship to material, device and dark diode parameters. Journal of Applied Physics 96, 2261–2271. https://doi.org/10.1063/1.1769092

Efaz, E.T., Rhaman, M.M., Imam, S.A., Bashar, K.L., Kabir, F., Mourtaza, M.E., Sakib, S.N., Mozahid, F.A., (2021). A review of primary technologies of thin-film solar cells. Engineering Research Express 3, 032001. https://doi.org/10.1088/2631-8695/ac2353

Fang, J., Chen, Z., Wang, N., Bai, L., Hou, G., Chen, X., Wei, C., Wang, G., Sun, J., Zhao, Y., Zhang, X., (2014). Improvement in performance of hydrogenated amorphous silicon solar cells with hydrogenated intrinsic amorphous silicon oxide p/i buffer layers. Solar Energy Materials and Solar Cells 128, 394–398. https://doi.org/10.1016/j.solmat.2014.06.012

Hamdani, D., Cahyono, Y., Yudoyono, G., Darminto, D., (2021). Performances analysis of heterojunction solar cells through integration of hydrogenated nanocrystalline silicon bilayer by using numerical study. Molecular Crystals and Liquid Crystals, 1–20. https://doi.org/10.1080/15421406.2021.1922226

Hao, L., Zhang, M., Ni, M., Shen, X., Feng, X., (2019). Simulation of a Silicon Heterojunction Solar Cell with a Gradient Doping Emitter Layer. Journal of Electronic Materials 48, 4688–4696. https://doi.org/10.1007/s11664-019-07241-3

Hernández-Como, N., Morales-Acevedo, A., (2010). Simulation of hetero-junction silicon solar cells with AMPS-1D. Solar Energy Materials and Solar Cells 94, 62–67. https://doi.org/10.1016/j.solmat.2009.05.021

Hua, X., Li, Z.P., Shen, W.Z., Xiong, G.Y., Wang, X.S., Zhang, L.J., (2012). Mechanism of Trapping Effect in Heterojunction With Intrinsic Thin-Layer Solar Cells: Effect of Density of Defect States. IEEE Transactions on Electron Devices 59, 1227–1235. https://doi.org/10.1109/TED.2012.2186139

Jensen, N., Hausner, R.M., Bergmann, R.B., Werner, J.H., Rau, U., (2002). Optimization and characterization of amorphous/crystalline silicon heterojunction solar cells. Progress in Photovoltaics: Research and Applications 10, 1–13. https://doi.org/10.1002/pip.398

Jia, R., Tao, K., Li, Q., Dai, X., Sun, H., Sun, Y., Jin, Z., Liu, X., (2017). Influence of using amorphous silicon stack as front heterojunction structure on performance of interdigitated back contact-heterojunction solar cell (IBC-HJ). Front. Energy 11, 96–104. https://doi.org/10.1007/s11708-016-0434-6

Kabbani, A., Shaik, H.M., (2021). PV Cell Parameters Modeling and Temperature Effect Analysis. International Journal of Renewable Energy Development 10, 563–571. https://doi.org/10.14710/ijred.2021.33845

Kouider, W.H., Belfar, A., (2020). Simulation and optimization of a-Si: H/µc-Si: H tandem solar cell with thinner active layers. Optik 223, 165594. https://doi.org/10.1016/j.ijleo.2020.165594

Lin, A., Ding, J., Yuan, N., Wang, S., Cheng, G., Lu, C., (2012). Analysis of the p window layer of thin film solar cells by simulation. Journal of Semiconductors 33, 023002. https://doi.org/10.1088/1674-4926/33/2/023002

Mehmood, H., Tauqeer, T., (2017). Modelling and performance analysis of amorphous silicon solar cell using wide band gap nc-Si:H window layer. IET Circuits, Devices & Systems 11, 666–675. https://doi.org/10.1049/iet-cds.2017.0072

Myong, S.Y., Lim, K.S., (2005). Natural hydrogen treatment effect during formation of double amorphous silicon-carbide p layer structures producing high-efficiency pin-type amorphous silicon solar cells. Applied Physics Letters 86, 033506. https://doi.org/10.1063/1.1853492

Park, J., Dao, V.A., Shin, C., Park, H., Kim, M., Jung, J., Kim, D., Yi, J., (2013). A buffer-layer/a-SiOx:H(p) window-layer optimization for thin film amorphous silicon based solar cells. Thin Solid Films 546, 331–336. https://doi.org/10.1016/j.tsf.2013.06.064

Park, J., Shin, C., Lee, S., Kim, S., Jung, J., Balaji, N., Dao, V.A., Lee, Y.-J., Yi, J., (2015). Effect of thermal annealing on the optical and electrical properties of boron doped a-SiOx:H for thin-film silicon solar cell applications. Thin Solid Films 587, 132–136. https://doi.org/10.1016/j.tsf.2015.01.062

Pham, D.P., Kim, S., Le, A.H.T., Park, J., Yi, J., (2018). Diminished band discontinuity at the p/i interface of narrow-gap a-SiGe:H solar cell by hydrogenated amorphous silicon oxide buffer layer. Journal of Alloys and Compounds 762, 616–620. https://doi.org/10.1016/j.jallcom.2018.05.248

Prayogi, S., Cahyono, Y., Iqballudin, I., Stchakovsky, M., Darminto, D., (2021). The effect of adding an active layer to the structure of a-Si: H solar cells on the efficiency using RF-PECVD. Journal of Materials Science: Materials in Electronics 32, 7609–7618. https://doi.org/10.1007/s10854-021-05477-6

Qiao, S., Chen, J., Liu, J., Zhang, X., Wang, S., Fu, G., (2016). Large lateral photovoltaic effect in µc-SiOx:H/a-Si:H/c-Si p–i–n structure. Applied Physics Express 9, 031301. https://doi.org/10.7567/apex.9.031301

Schmidt, M., Schoepke, A., Korte, L., Milch, O., Fuhs, W., (2004). Density distribution of gap states in extremely thin a-Si:H layers on crystalline silicon wafers. Journal of Non-crystalline Solids 338, 211–214.

Stangl, R., Leendertz, C., Haschke, J., (2010). Numerical Simulation of Solar Cells and Solar Cell Characterization Methods: the Open-Source on Demand Program AFORS-HET, in: Rugescu, R.D. (Ed.), Solar Energy. IntechOpen, Rijeka. https://doi.org/10.5772/8073